Nano Research
2020, 13(1): 188–195

ISSN 1998-0124 CN 11-5974/O4
https://doi.org/10.1007/s12274-019-2594-2

Highly dispersed Co-Mo sulfide nanoparticles on reduced graphene oxide for lithium and sodium ion storage

Yuqing Liao[1], Chun Wu[2], Yaotang Zhong[1], Min Chen[1], Luyang Cai[1], Huirong Wang[1], Xiang Liu[1,3,4] (✉), Guozhong Cao[5] (✉), and Weishan Li[1,3] (✉)

[1] *School of Chemistry, South China Normal University, Guangzhou 510006, China*
[2] *College of Materials Science and Engineering, Changsha University of Science and Technology, Changsha 410114, China*
[3] *National and Local Joint Engineering Research Center of MPTES in High Energy and Safety LIBs, Engineering Research Center of MTEES (Ministry of Education), and Key Lab. of ETESPG(GHEI), South China Normal University, Guangzhou 510006, China*
[4] *School of Energy Science and Engineering, Nanjing Tech University, Nanjing 211816, China*
[5] *Department of Materials Science and Engineering, University of Washington, Seattle, Washington 98195, USA*

Received: 11 August 2019 / **Revised:** 16 October 2019 / **Accepted:** 6 November 2019

ABSTRACT

A novel hybrid, highly dispersed spinel Co-Mo sulfide nanoparticles on reduced graphene oxide ($Co_3S_4/CoMo_2S_4$@rGO), is reported as anode for lithium and sodium ion storage. The hybrid is synthesized by one-step hydrothermal method but exhibits excellent lithium and sodium storage performances. The as-synthesized $Co_3S_4/CoMo_2S_4$@rGO presents reversible capacity of 595.4 mA·h·g^{-1} and 408.8 mA·h·g^{-1} after 100 cycles at a current density of 0.2 A·g^{-1} for lithium and sodium ion storages, respectively. Such superior performances are attributed to the unique composition and structure of $Co_3S_4/CoMo_2S_4$@rGO. The rGO provides a good electronically conductive network and ensures the formation of spinel $Co_3S_4/CoMo_2S_4$ nanoparticles, the $Co_3S_4/CoMo_2S_4$ nanoparticles provide large reaction surface for lithium and sodium intercalation/deintercalation, and the spinel structure allows fast lithium and sodium ion diffusion in three dimensions.

KEYWORDS

Co-Mo sulfide, nanoparticle, reduced graphene oxide, lithium and sodium ion storage

1 Introduction

With the increasing consumption of fossil fuels and serious environmental pollution, energy storage systems for renewable energy utilization have attracted more and more attentions. Rechargeable lithium-ion batteries (LIBs) have been widely used as power sources for portable electronic devices and electric vehicles due to their high energy density and environmental friendliness, but their high cost restricts their applications in large scale energy storage [1, 2]. Recently, due to the low cost and abundant resources of sodium, sodium ion batteries (SIBs) have attracted increasing attention, which is undoubtedly the most potential alternative to LIBs [3–14]. It is well known that SIBs share a similar working principle with LIBs due to their similar electrochemical potential, which makes it possible to use the same electrode materials for both LIBs and SIBs. Current graphite anode in LIBs has a limited theoretical capacity of 372 mA·h·g^{-1} and is not suitable for sodium ion storage due to the electrochemically irreversible intercalation of sodium ions [9, 15]. Therefore, searching for the alternatives to graphite anode becomes a hot research topic in advancing LIBs and SIBs [1, 9, 16–24].

Hybrid metal oxides, such as $CoMoO_4$ [25–28], $ZnCo_2O_4$ [27], $ZnMn_2O_4$ [29, 30], $CoMn_2O_4$ [31], $NiCo_2O_4$ [32–34], $MnCo_2O_4$ [35], and $CuCo_2O_4$ [36] have been studied as anode materials for LIBs due to their better electrochemical performance than the single metal oxide. For example, it has previously been reported that porous $ZnMn_2O_4$ nanospheres synthesized by a facile microemulsion method provided a reversible lithium storage capacity of 300 mA·h·g^{-1} at 6,000 mA·g^{-1} and yielded a capacity retention of 91% after 120 cycles at 200 mA·g^{-1} [30]. Double-shelled $CoMn_2O_4$ hollow microcubes, synthesized via a facile co-precipitation and annealing method, manifested a high specific capacity (830 mA·h·g^{-1} at a current density of 200 mA·g^{-1}) and good cycling performance (retaining 624 mA·h·g^{-1} after 50 cycles) as anode for LIBs [31]. Obviously, the cyclic stability of these hybrid metal oxides is not satisfactory.

Comparatively, metal sulfides provide better cyclic stability as anodes for either LIBs or SIBs besides of their merit of high theoretical capacity [2, 9, 18, 37–45]. Recently, their hybrids such as Co-Mo sulfides have been shown to have excellent electrocatalytic activity toward oxidation or reduction reactions [46, 47], but are rarely considered for the application in LIBs and SIBs [19, 48]. Herein, we report a novel anode ($Co_3S_4/CoMo_2S_4$@rGO) that can be used simultaneously for LIBs and SIBs, which are fabricated by highly dispersing Co-Mo sulfides ($Co_3S_4/CoMo_2S_4$) nanoparticles on three-dimensional (3D) reduced graphene oxide (rGO) sheets via a one-step hydrothermal reaction. It is found that morphology of Co-Mo sulfides depends on the dosage of graphene oxide and spinel nanoparticles uniformly dispersed in rGO can be achieved by using 3 mg·mL^{-1}

Address correspondence to Xiang Liu, iamxliu@njtech.edu.cn; Guozhong Cao, gzcao@u.washington.edu; Weishan Li, liwsh@scnu.edu.cn

graphene oxide in the fabrication of $Co_3S_4/CoMo_2S_4$@rGO. In the resulting $Co_3S_4/CoMo_2S_4$@rGO, the rGO provides a good electronically conductive network and a soft support for buffering volume change, the hybrid $Co_3S_4/CoMo_2S_4$ contributes to capacity through the redox reactions of bimetal ions, and the nanoparticles provide large reaction surface for lithium and sodium intercalation/deintercalation. Additionally, the resulting $Co_3S_4/CoMo_2S_4$ nanoparticles exhibit a spinel structure that allows lithium and sodium ions to diffuse in three dimensions. Consequently, the $Co_3S_4/CoMo_2S_4$@rGO presents excellent electrochemical performances for either LIBs or SIBs.

2 Experimental

2.1 Synthesis of graphene oxide

Graphene oxide (GO) was prepared by a modified Hummers method. Typically, natural graphite flakes (2 g, Sigma-Aldrich) and sodium nitrate (2 g, Kemiou Chemical Reagent Ltd., Tianjin) were added in concentrated sulfuric acid (98%, 46 mL, Chemical Reagent Ltd.) under vigorous stirring in an ice water bath. Subsequently, potassium permanganate (99.5%, 6 g, Kemiou Chemical Reagent Ltd., Tianjin) was slowly added. The mixture was kept at the temperature below 20 °C for 90 min under stirring and then at 35 °C for another 90 min. 80 mL of distilled water was added dropwise to the mixture under vigorous stirring at 98 °C for 30 min. Finally, 20 mL of H_2O_2 (30 wt.%, Chemical Reagent Ltd., Tianjin) was added. The bright yellow suspension was harvested, washed 10 times with HCl (1:6 v/v, Chemical Reagent Ltd.) and water and dried under vacuum at 60 °C for 24 h to obtain solid GO [49].

2.2 Preparation of $Co_3S_4/CoMo_2S_4$@rGO

The preparation process of $Co_3S_4/CoMo_2S_4$@rGO was similar to the previous reports [48, 50], but the formation of $Co_3S_4/CoMo_2S_4$ nanoparticles was specially considered, as illustrated in Scheme 1. First, the synthesized GO was dispersed in water with various contents of GO (n = 1, 3, 5, and 7 mg·mL^{-1}) for 3 h under ultrasonication (KQ-300DA) to yield a brown colloidal solution. Then, 3 mmol of $Na_2MoO_4·2H_2O$, 3 mmol of $Co(NO_3)_2·6H_2O$ and 12 mmol of thiourea (Tu) were added to the above GO solution under stirring for 1 h. 6 mL of ethylenediamine (En) was added to the mixture, and then the mixture was transferred to a 100 mL Teflon-lined autoclave. After hydrothermal reaction at 200 °C for 24 h, the products were washed several times with ethanol and deionized water, and then freeze-dried for 48 h, denoted as $Co_3S_4/CoMo_2S_4$@rGO-n. $Co_3S_4/CoMo_2S_4$ was also prepared for comparison without using GO.

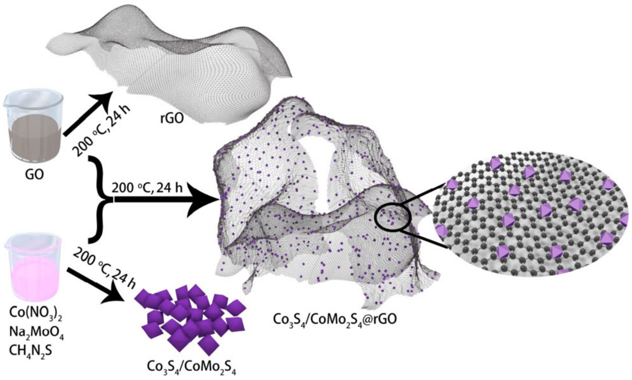

Scheme 1 Schematic illustration on the fabrication of highly dispersed Co-Mo sulfide hybrid nanoparticles on reduced graphene oxide ($Co_3S_4/CoMo_2S_4$@rGO).

All reagents were of analytical grade and used without further purification. Deionized water is required for each step, including preparation in the aqueous solution and washing products.

2.3 Materials characterization

X-ray diffraction (XRD) patterns were collected at room temperature with a D/MAX 2200 VPC X-ray generator using Cu-Kα (λ = 1.5406 Å) radiation at a step of 10°·min^{-1} from 10° to 80°. Thermogravimetric analysis (TGA) data were obtained with an STA409PC Diamond TG-DTA thermal analyzer over a temperature range of 30 to ~ 800 °C in air at a heating rate of 10 °C·min^{-1}. The morphology, microstructure and components of the samples were examined by scanning electron microscopy (SEM) on a FEI Quanta 250 FEG, and transmission electron microscope (TEM) on a JEM-2100. The specific surface area and pore size distribution of the samples were determined using Brunauer–Emmett–Teller method (BET, ASAP-2020, Micromeritics, USA). X-ray photoelectron spectroscopy (XPS) was conducted on a K-Alpha X-ray photoelectron spectrometer (Thermo fisher Scientific, USA).

2.4 Electrochemical measurements

The electrochemical performance of the samples was evaluated using a standard CR2032 coin-type cells. To prepare the electrode, 80 wt.% of active material, 10 wt.% of conductive super-P carbon, 10 wt.% of poly-(vinylidene fluoride) (PVDF, Sigma Aldrich) as a binder, were mixed in N-methyl-2-pyrrolidone (NMP). The mixed slurry was coated on a copper foil using the Doctor-Blade technique, dried at 120 °C under vacuum overnight, and pressed at 20 MPa for 10 s. The resulting copper foil was cut into disk electrodes. The mass density of the active material in each electrode was 1.0 to 2.0 mg·cm^{-2}. For LIB test, a Li disk was used as a counter electrode, the commercial Celgard 2400 film was employed as the separator, and the electrolyte was 1 M $LiPF_6$ in a mixed solvent of ethylene carbonate (EC), diethyl carbonate (DEC), and dimethyl carbonate (DMC) (EC:DEC:DMC = 1:1:1, v/v). For SIB test, a Na disk was used as a counter electrode, a glass fiber filter (GB-100R, Advantec, Japan) was used as the separator, and the electrolyte was 1 M $NaClO_4$ in EC/DEC solution (1:1, v/v) containing 5% fluoroethylene carbonate. Electrochemical measurements were made 12 h after battery assembly. Cyclic voltammetry (CV) was performed at room temperature using a CHI760e electrochemical station (Shanghai Chenhua, China). Electrochemical impedance spectroscopy (EIS) was performed on a PGSTAT-30 workstation (Autolab, Switzerland) with AC signals of 5 mV from 100 kHz to 0.01 Hz. Galvanostatic charge/discharge tests were carried out at current densities of 0.1–5 A·g^{-1} between 0.01 and 3 V using a battery analyzer (Land CT2001A, Wuhan, China).

3 Results and discussion

3.1 Physical properties

As shown in Fig. S1 in the Electronic Supplementary Material (ESM), the XRD patterns of $Co_3S_4/CoMo_2S_4$@rGO-n (n = 1, 3, 5, 7) are similar except that the intensity of peaks corresponding to the (200) and (201) planes of $CoMo_2S_4$ shows a first increase and a latter decrease as the content of GO increases. Especially, these peaks disappear when the content of GO is higher than 3 mg·mL^{-1}. This change suggests that the content of GO affects the particle size of the resulting products.

The SEM and TEM images of $Co_3S_4/CoMo_2S_4$@rGO-n (n = 1, 3, 5, 7) are presented in Fig. S2 in the ESM, which indicate the change in morphology of these samples. When the content of GO is 1 mg·mL^{-1}, the sample is composed of fine nanosheets and a small amount of spinel. When the content of GO is increased to 3 mg·mL^{-1}, spinel nanoparticles uniformly dispersed in graphene can be identified. When the content of GO is further increased, the nanoparticles become finer and finer, while the amount of nano-sheet structure is increased and finally only the nanosheets can be seen. This change can be explained by the active sites that graphene provides for Co-Mo sulfide growth. More active sites are available with using more graphene, which are beneficial for the formation of smaller particles. On the other hand, nanosheets will be more easily formed with larger content of graphene. Considering the uniform nanoparticle size of the sample resulting from 3 mg·mL^{-1} GO, further investigations are focused on this sample (Co_3S_4/$CoMo_2S_4$@rGO-3), denoted as Co_3S_4/$CoMo_2S_4$@rGO.

The crystal structure of the as-prepared rGO, Co_3S_4/$CoMo_2S_4$ and Co_3S_4/$CoMo_2S_4$@rGO was determined by XRD. The obtained XRD patterns are shown in Fig. 1. The peaks at 32.7, 38.2, 47.3, 55.1, and 75.4 correspond to the *(222), *(400), *(422), *(440), *(642) crystal planes of Co_3S_4 (JCPDS card no. 75-1561), respectively, while the peaks of the #(200), #(001), #(201), #(400), #(310), #(401), #($\bar{2}$03), #($\bar{7}$12) and #(022) planes located at 15.3, 17.4, 28.4, 31.1, 35.9, 42.9, 47.2, 57.3 and 67.7, respectively, are consistent with $CoMo_2S_4$ (JCPDS card no. 74-0537) [48]. In addition, the broad diffraction peak at around 25.2 corresponds to the ∇ (002) plane of graphene. The distinct diffraction peaks of Co_3S_4/$CoMo_2S_4$ and graphene confirm the composition of Co_3S_4/$CoMo_2S_4$@rGO. When Mo is not introduced, only CoS_2 can be identified (the resulting sample is denoted as CoS_2, Fig. S3 in the ESM), suggesting that the introduction of Mo favors the formation of Co_3S_4/$CoMo_2S_4$ on rGO.

Figure 2 shows the SEM and TEM images of the rGO, Co_3S_4/$CoMo_2S_4$ and Co_3S_4/$CoMo_2S_4$@rGO, along with high resolution TEM (HRTEM) and selected area electron diffraction (SAED) pattern of Co_3S_4/$CoMo_2S_4$@rGO. The graphene network can be seen from the SEM image in Fig. 2(a). Without rGO, as shown in Fig. 2(b), the Co_3S_4/$CoMo_2S_4$ is mainly of spinel particles from nano to micro sizes, together with a small amount of sheet particles. When rGO is introduced, as shown in Figs. 2(c), 2(d), and 2(e), uniform spinel Co_3S_4/$CoMo_2S_4$ nanoparticles that are highly dispersed on rGO are achieved. From the elemental mappings (Fig. S4 in the ESM), it can be found that elements of Co, Mo and S are mainly distributed in the whole Co_3S_4/$CoMo_2S_4$ nanoparticles of Co_3S_4/$CoMo_2S_4$@rGO. The HRTEM in Fig. 2(f) gives a straightforward observation of the Co_3S_4/$CoMo_2S_4$@rGO. The fringes with inter-planar distances of 0.34, 0.24, 0.58 and 0.31 nm, attributed to the (002) plane of reduced graphene oxide, the (400) plane of Co_3S_4 and the (200) and (201) planes of $CoMo_2S_4$, respectively, can be identified, which are in agreement with the XRD results. The SAED pattern of the sample exhibits bright crystalline rings (Fig. 2(f)), which matches well with the (002), (020) planes of $CoMo_2S_4$, and (511) planes of Co_3S_4, further confirming that the Co_3S_4/$CoMo_2S_4$@rGO hybrid possesses a crystal structure of orthorhombic Co_3S_4/$CoMo_2S_4$. This unique configuration is beneficial for improving rate capability and cyclic stability of batteries: Co_3S_4/$CoMo_2S_4$ nanoparticles provide not only large surface area for ion insertion/extraction, but also short path for ion diffusion in particles; the rGO provide electronically conductive network and functions as support for stabilizing Co_3S_4/$CoMo_2S_4$ nanoparticles; and the spinel structure provides a 3D path for ion diffusion in particles.

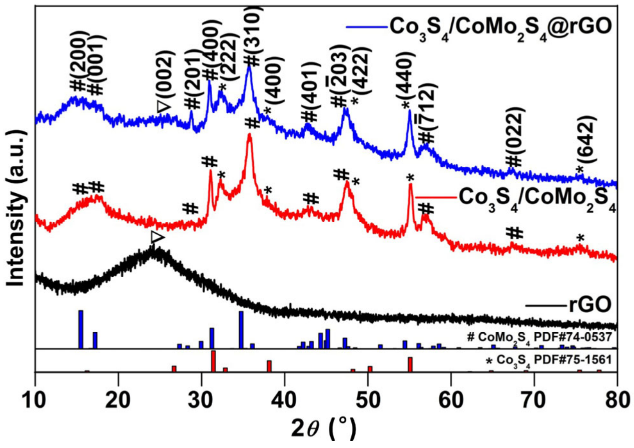

Figure 1 XRD patterns of rGO, Co_3S_4/$CoMo_2S_4$ and Co_3S_4/$CoMo_2S_4$@rGO.

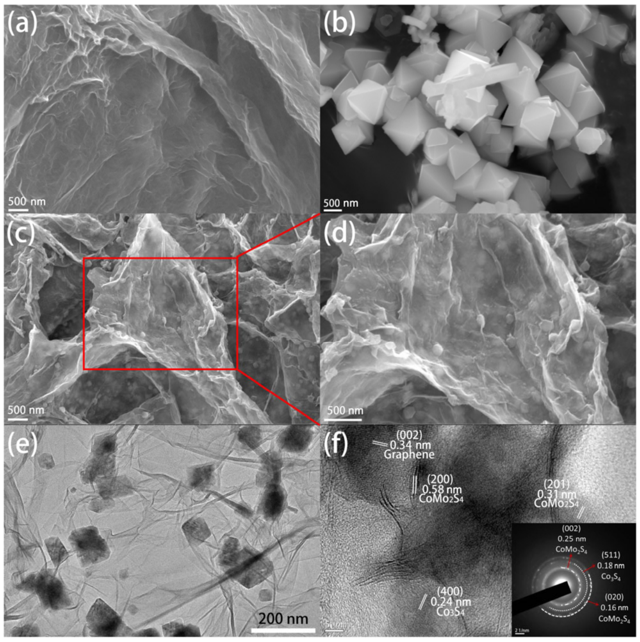

Figure 2 SEM images of (a) rGO, (b) Co_3S_4/$CoMo_2S_4$, ((c) and (d)) Co_3S_4/$CoMo_2S_4$@rGO. (e) TEM and (f) HRTEM images of Co_3S_4/$CoMo_2S_4$@rGO. The inset in (f) is the SAED pattern of Co_3S_4/$CoMo_2S_4$@rGO.

To determine the content of rGO in the samples, TGA was conducted on rGO, Co_3S_4/$CoMo_2S_4$ and Co_3S_4/$CoMo_2S_4$@rGO (Fig. S5 in the ESM). Three major steps of weight loss are observed in the TGA curve of rGO: below 100, 100–620 and 620–800 °C. The weight loss below 100 °C is attributed to the removal of adsorbed water, while the weight loss between 100 and 620 °C is ascribed to the combustion of graphite carbon. Compared with rGO, Co_3S_4/$CoMo_2S_4$ and Co_3S_4/$CoMo_2S_4$@rGO exhibits lower mass loss over the range of 100–620 °C, which is mainly attributed to the combustion of graphene, the conversion of sulfides into sulfites, the decomposition of sulfites into oxides, and the oxidation of sulfites to sulfates [9]. The weight loss from 620 to 800 °C was ascribed to the decomposition of the sulfates [1, 9]. Based on the weight loss below 620 °C of Co_3S_4/$CoMo_2S_4$@rGO, the content of graphene in Co_3S_4/$CoMo_2S_4$@rGO is less than 36.4%.

The specific surface area of the Co_3S_4/$CoMo_2S_4$ and Co_3S_4/$CoMo_2S_4$@rGO was obtained from the N_2 adsorption–desorption isotherms (Fig. S6 in the ESM). Co_3S_4/$CoMo_2S_4$ exhibits a small surface area of 0.9 m^2·g^{-1}, while Co_3S_4/$CoMo_2S_4$@rGO has a specific surface area of 60.5 m^2·g^{-1}, indicative of the contribution of rGO. The effect of GO content on the surface area and pore sizes of the products was also investigated by N_2 adsorption–desorption isotherms. As shown in Fig. S7(a) in the ESM, the samples $Co_3S_4/CoMo_2S_4$@rGO-n (n = 1, 3, 5, 7) have similar adsorption–desorption behavior, suggesting the chemical similarity of the sample. The calculated BET surface area is 56.7, 60.5, 68.4 and 55.9 $m^2 \cdot g^{-1}$ and the average pore size (Fig. S7(b) in the ESM) is 5.9, 6.1, 7.1 and 6.2 nm for the samples $Co_3S_4/CoMo_2S_4$@rGO-n (n = 1, 3, 5, 7), respectively. The far larger surface area of $Co_3S_4/CoMo_2S_4$@rGO-n (n = 1, 3, 5, 7) than $Co_3S_4/CoMo_2S_4$ suggests that the rGO contributes to the major surface area. The slight difference in surface area and pore size among samples of $Co_3S_4/CoMo_2S_4$@rGO-n (n = 1, 3, 5, 7) can be ascribed to the different morphologies of $Co_3S_4/CoMo_2S_4$ particles on rGO, which can be neglected compared to the contribution of rGO.

XPS was performed to further confirm the presence of Co_3S_4 and $CoMo_2S_4$. The C 1s spectrum can be split into three peaks of 284.8 (C=C), 285.9 (C–O), 287.1 (C=O), and 288.8 (O–C=O) eV (Fig. 3(a)), suggesting the presence of oxygen-containing groups in rGO skeleton. The Co 2p spectrum (Fig. 3(b)) can be deconvoluted into two spin-orbit doublets and two shakeup satellites. The first doublet at 778.86, 794.28 eV, and the second at 781.88, 796.98 eV are assigned to Co^{3+} and Co^{2+}, respectively [48, 51, 52]. The binding energies of Mo $3d_{3/2}$ and Mo $3d_{5/2}$ are 232.54 and 228.88 eV, respectively (Fig. 3(c)). The presence of S can be indicated by the S 2s peak at 226.13 eV and the S 2p peaks at 163.94 and 161.63 eV attributed to the S $2p_{1/2}$ and S $2p_{3/2}$, respectively (Fig. 3(d)).

3.2 Electrochemical performance

The cycle performance of $Co_3S_4/CoMo_2S_4$@rGO-n (n = 1, 3, 5, 7) for sodium ion storage at a current density of 0.2 $A \cdot g^{-1}$ is shown in Fig. S8 in the ESM, indicating that all the samples can store sodium ions and outperform CoS_2@rGO (Fig. S9 in the ESM). The charge transfer characteristics of $Co_3S_4/CoMo_2S_4$@rGO-n (n = 1, 3, 5, 7) were studied by electrochemical impedance spectroscopy. The obtained impedance spectra are shown in Fig. S10 in the ESM, which consist of a pressed semicircle at high frequencies, corresponding to the impedance of charge transfer (R_{ct}) and the ion transportation in the solid electrolyte interphase (SEI) (R_f), and a straight line at low-frequency region, corresponding to ion diffusion. All the electrodes have similar interface resistance ($R_{ct} + R_f$) values before cycling. However, $Co_3S_4/CoMo_2S_4$@rGO-3 exhibits the lowest one among all the samples after the first cycle, suggesting that the $Co_3S_4/CoMo_2S_4$@rGO-3 has faster electrochemical reaction kinetics. As expected, $Co_3S_4/CoMo_2S_4$@rGO ($Co_3S_4/CoMo_2S_4$@rGO-3) exhibits the best electrochemical performance, which is related to its special configuration, spinel $Co_3S_4/CoMo_2S_4$ nanoparticles highly dispersed on electronically conductive rGO. Similarly, $Co_3S_4/CoMo_2S_4$@rGO shows superior lithium ion storage ability in terms of capacity delivery and cycle stability, especially when compared with $Co_3S_4/CoMo_2S_4$ and rGO (Fig. S11 in the ESM). $Co_3S_4/CoMo_2S_4$ is good in lithium storage (Fig. S11(a) in the ESM) but poor in sodium storage (Fig. S11(b) in the ESM). This difference can be explained by the larger radius of sodium ion than lithium ion. However, $Co_3S_4/CoMo_2S_4$@rGO is excellent either in lithium or sodium storage, suggesting the importance of introducing suitable content of rGO, which not only provides an electronically conductive network, but also ensures the formation of spinel nanoparticles. For LIBs, $Co_3S_4/CoMo_2S_4$@rGO achieves a discharge capacity of 594.5 $mA \cdot h \cdot g^{-1}$ and a capacity retention of over 90.5% at a current density of 0.2 $A \cdot g^{-1}$ after 100 cycles, compared to the 266.2 and 47.9 $mA \cdot h \cdot g^{-1}$ for rGO and $Co_3S_4/CoMo_2S_4$, respectively. For SIBs, rGO and $Co_3S_4/CoMo_2S_4$ only delivers 84.8 and 55.6 $mA \cdot h \cdot g^{-1}$ at a current density of 0.2 $A \cdot g^{-1}$ after 100 cycles, respectively, much inferior to $Co_3S_4/CoMo_2S_4$@rGO (408.8 $mA \cdot h \cdot g^{-1}$). These performances of $Co_3S_4/CoMo_2S_4$@rGO are the best among currently reported materials used for lithium or sodium ion storage (Table S1 in the ESM).

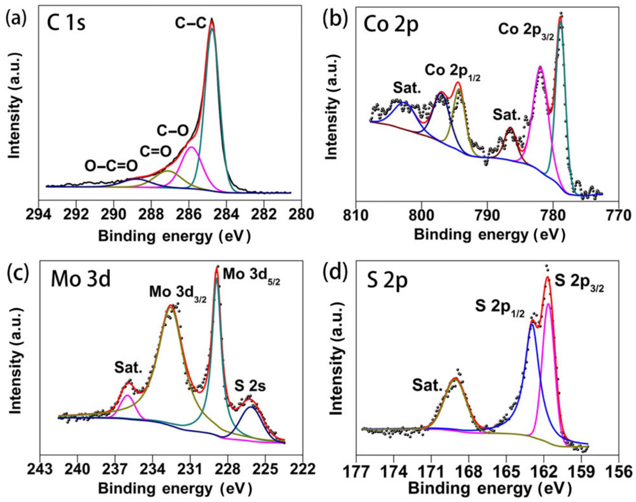

Figure 3 Typical XPS profiles of C 1s (a), Co 2p (b), Mo 3d (c) and S 2p (d) in $Co_3S_4/CoMo_2S_4$@rGO.

Figure 4 shows the CV curves of $Co_3S_4/CoMo_2S_4$@rGO electrode in the solution with $LiPF_6$ for the first five cycles in the voltage range from 0.01 to 3 V vs. Li / Li^+ at a scan rate of 0.2 $mV \cdot s^{-1}$ (Fig. 4(a)), together with *ex situ* XPS patterns of Co 2p (Fig. 4(b)) and Mo 3d (Fig. 4(c)) at different peak potentials during the first discharge (cathodic) process. There are four cathodic peaks appearing at around 1.55, 1.15, 0.72, and 0.36 V, respectively, in the first CV curve. In the Co 2p spectrum at 1.55 V, the spin-orbit doublet peaks of Co^{3+} at 778.86, 794.28 eV disappear, suggesting that Co^{3+} is reduced to Co^{2+} at about 1.55 V. At 0.36 V, the spin-orbit doublet peaks of Co^{2+} at 781.88 and 796.98 eV nearly disappear, which can be attributed to the reduction of Co^{2+} to Co. On the other hand, the binding energy of Mo $3d_{5/2}$ is weakened from 1.55 to 0.72 V, suggesting that the peak potential peaks of 1.55 and 1.15 V involve the reduction of Mo ions corresponding to the Li^+ insertion into $CoMo_2S_4$ ($CoMo_2S_4 + y\ Li^+ + y\ e^- \rightarrow Li_yCoMo_2S_4$). At 0.72V, the spin-orbit doublet peaks of Mo 3d spectrum at 232.54 and 228.88 eV nearly disappear, suggesting that this peak potential is related

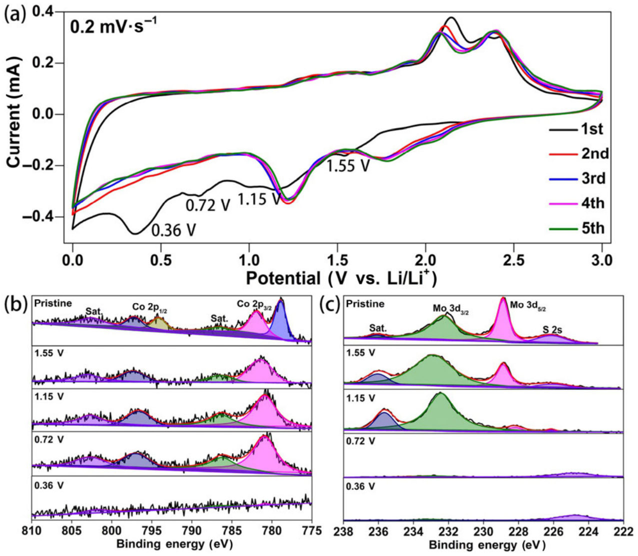

Figure 4 (a) CV curves of $Co_3S_4/CoMo_2S_4$@rGO electrode in EC/DEC/DMC solution with $LiPF_6$ (EC:DEC:DMC = 1:1:1, v/v) at 0. 2 $mV \cdot s^{-1}$. *Ex situ* XPS patterns of (b) Co 2p and (c) Mo 3d at different peak potentials of the first CV curve in (a).

to the conversion reaction of $Li_yCoMo_2S_4$ to Mo. During the charge (anodic) scan, the peaks at 2.08 and 2.29 V in CV curves are related to the oxidation of Co and Mo. In the following discharge scans, the original cathodic peaks disappear while new peaks appear at 1.28 and 1.79 V, suggesting the following lithiation processes involve only two step reductions. No significant changes in the redox peaks are observed, indicating the outstanding lithiation/delithiation stability of Co_3S_4/$CoMo_2S_4$@rGO electrode. It can be noted that the cathodic current for the first cycle is apparently larger than those for the following cycles. This difference can be attributed to the formation of a SEI [53, 54].

To further investigate the lithiation/delithiation mechanism of the Co_3S_4/$CoMo_2S_4$@rGO, *in situ* XRD analysis was performed during the initial discharge/charge processes at a current rate of 0.1 $A\cdot g^{-1}$ between 0.01 and 3.0 V. As presented in Fig. 5, the diffraction peaks of the fresh electrode can be assigned to the Co_3S_4/$CoMo_2S_4$@rGO. When the cell is discharged from 3.0 to 1.55 V, the typical diffraction peaks of Co_3S_4 disappear, while new peaks are observed at 35.3 and 54.6, corresponding to the (101) and (110) planes of CoS (JCPDS card no. 75-0605), respectively. From 1.55 to 1.15 V, the crystalline phases of $CoMo_2S_4$ and CoS are almost identical, corresponding to Li^+ ion insertion process. The peaks at 27.1 and 65.5 correspond to the (101) planes of Li_2S (JCPDS card no. 77-2145) and the (220) plane of Mo (JCPDS card no. 88-2331) gradually appears below 1.15 V. When the cell is discharged from 0.72 to 0.01 V, the typical diffraction peaks of $CoMo_2S_4$ and CoS disappear, while the peaks of Li_2S and Mo become stronger along with the discharge voltage decrease, indicating the continuously proceeding conversion reaction of Li^+ ions with $CoMo_2S_4$ and CoS. These structure identifications are completely consistent with the XPS analysis of Co 2p and Mo 3d in Figs. 4(b) and 4(c) at different peak potentials during the initial discharge. During the charging process, the peaks of Li_2S diminishes gradually, along with the appearance of weak peaks at 31.1, 35.3 and 54.6, which can be ascribed to the (400) planes of $CoMo_2S_4$ and the (101), (110) planes of CoS, respectively, and are consistent with the XPS pattern of Co 2p from Co_3S_4/$CoMo_2S_4$@rGO electrode at 3.0 V during the first charge (anodic) process (Fig. 4(a)). CoS has only spin-orbit doublet peak of Co^{2+} at 781.65 and 797.51 eV. Therefore, the Li^+-storage mechanism of Co_3S_4/$CoMo_2S_4$@rGO mainly involves following reversible reactions (Eqs. (2) and (3)), corresponding to the two couples of redox peaks in the CV curves of Fig. 4.

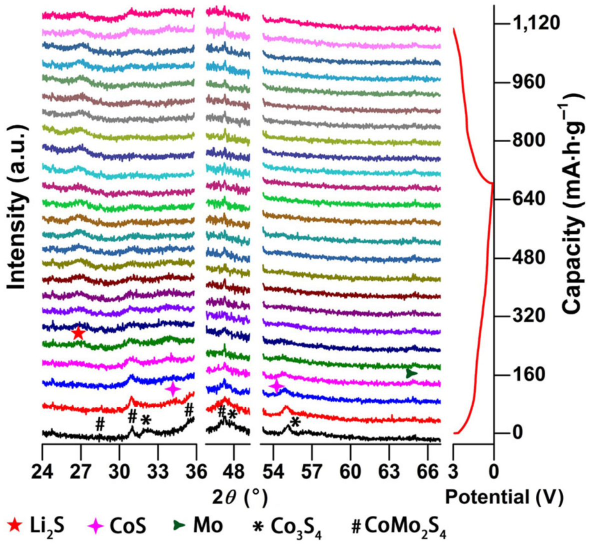

Figure 5 *In situ* XRD patterns of lithiation/delithiation mechanism of Co_3S_4/$CoMo_2S_4$@rGO during the initial cycle at a current rate of 0.1 $A\cdot g^{-1}$ between 0.01 and 3.0 V.

$$Co_3S_4 + 2Li^+ + 2e^- \rightarrow 3CoS + Li_2S \tag{1}$$

$$x\,Li^+ + xe^- + CoS \leftrightarrow Li_xCoS \leftrightarrow Li_xS + Co \tag{2}$$

$$y\,Li^+ + y\,e^- + CoMo_2S_4 \leftrightarrow Li_yCoMo_2S_4 \leftrightarrow 4Li_{\frac{y}{4}}S + Co + 2Mo \tag{3}$$

The typical charge–discharge curves of Co_3S_4/$CoMo_2S_4$@rGO at 0.2 $A\cdot g^{-1}$ are shown in Fig. 6(a). The initial discharge and charge capacities are 1,027.1 and 721.6 $mA\cdot h\cdot g^{-1}$, respectively. The Coulombic efficiency (CE) is 70.25%, suggesting the formation of SEI from the electrolyte decomposition. During the subsequent cycles the CE quickly is increased to 93.68% in the second cycle and kept at almost 100%. From the sixth cycle onward, Co_3S_4/$CoMo_2S_4$@rGO sustains a reversible capacity of as high as 594.5 $mA\cdot h\cdot g^{-1}$ even after 100 cycles at 0.2 $A\cdot g^{-1}$, presenting a capacity retention of 90.5% (Fig. 6(b)). Even at a

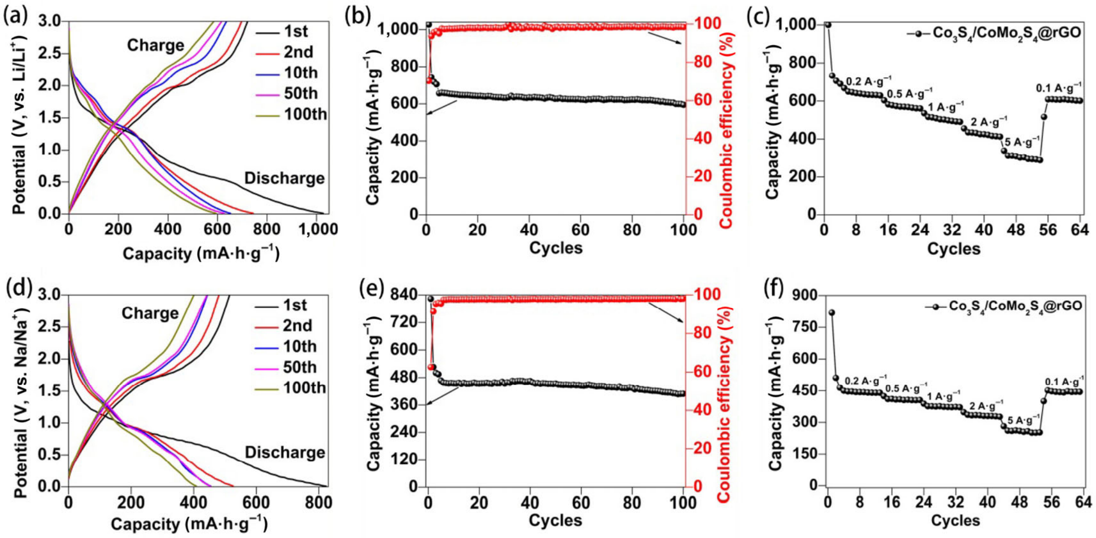

Figure 6 Charge/dicharge performances of Co_3S_4/$CoMo_2S_4$@rGO electrode in EC/DEC/DMC solution with $LiPF_6$ (EC:DEC:DMC = 1:1:1, v/v) ((a)–(c)) and EC/DEC solution (1:1, v/v) with 1 M $NaClO_4$ ((d)–(f)): ((a) and (d)) galvanostatic charge–discharge profiles, ((b) and (e)) cycling stability at a current density of 0.2 $A\cdot g^{-1}$ and ((c) and (f)) rate capability.

higher current density of 1 A·g^{-1}, it still delivers a specific capacity of 432.6 mA·h·g^{-1} with a capacity retention of 86.9% after 100 cycles (Fig. S13 in the ESM), confirming the contribution of highly dispersed spinel Co_3S_4/$CoMo_2S_4$ nanoparticles on rGO to the improved electronic conductivity and the enhanced electrochemical reaction kinetics. The rate capability of Co_3S_4/$CoMo_2S_4$@rGO is shown in Fig. 6(c). As the current density is increased from 0.1 to 0.2, 0.5, 1, 2 and 5 A·g^{-1}, the specific capacity of 649, 582, 516, 435, and 312 mA·h·g^{-1} is achieved correspondingly. When the current density is turned back to 0.1 A·g^{-1}, a capacity of as high as 609 mA·h·g^{-1} can be recovered. Apparently, Co_3S_4/$CoMo_2S_4$@rGO is attractive when used as anode of LIBs.

The CV curves of Co_3S_4/$CoMo_2S_4$@rGO in the electrolyte containing $NaClO_4$ are presented in Fig. S14 in the ESM, which are similar to those in the electrolyte containing $LiPF_6$ (Fig. 4(a)), although the number of peaks is different. In the first discharge process, the peaks at around 0.85 and 0.50 V are assigned to the intercalation of sodium ions into Co_3S_4/$CoMo_2S_4$@rGO and the conversion of Co_3S_4/$CoMo_2S_4$@rGO to Co and Mo along with Na_2S, respectively. The apparently large cathodic current in the first cycle than those in the following cycles suggests the formation of SEI [1, 43, 55]. The peaks at 1.78 and 2.05 V in the anodic process are related with the oxidation of Co and Mo and Na_2S.

Co_3S_4/$CoMo_2S_4$@rGO also presents excellent performance as anode of SIBs. The charge–discharge profiles (Fig. 6(d)) for sodium ion storage are similar to those for lithium ion storage, but with lower voltage plateaus and lower capacities, which are due to the difference in energy barriers for the insertion and extraction of lithium and sodium ions. Due to the bigger ionic radius of Na^+ than Li^+, the kinetics of sodium insertion and extraction is slower compared to lithium. The initial discharge and charge capacity is 823.0 and 514.6 mA·h·g^{-1}, respectively, with a CE of 62.5 %. A high CE of over 97.5% is achieved after 6 cycles. After 100 cycles at a current density of 0.2 A·g^{-1}, a discharge capacity of 408.8 mA·h·g^{-1} is retained with a capacity retention of 89.3% (Fig. 6(e)). At a higher current density of 1.0 A·g^{-1}, a capacity of as high as 317.2 mA·h·g^{-1} with a capacity retention of 78.2% is maintained after 100 cycles (Fig. S15 in the ESM). The specific capacity is 443, 408, 375, 333 and 258 mA·h·g^{-1} when the current density is varied from 0.1 to 0.2, 0.5, 1.0, 2.0 and 5.0 A·g^{-1}, respectively, and is recovered to 451 mA·h·g^{-1} when the current density is switched back to 0.1 A·g^{-1} (Fig. 6(f)). The TEM images of the Co_3S_4/$CoMo_2S_4$@rGO after 100 cycles (Fig. S16 in the ESM) show that the Co_3S_4/$CoMo_2S_4$ nanoparticles remain unchanged, illustrating the structure stability of Co_3S_4/$CoMo_2S_4$ nanoparticles. These results demonstrate that Co_3S_4/$CoMo_2S_4$@rGO can serve anodes not only for LIBs but also for SIBs.

4 Conclusions

A binary-ternary compound hybrid, Co_3S_4/$CoMo_2S_4$@rGO, has been successfully synthesized by one-step hydrothermal method. When applied as anodes for LIBs and SIBs, Co_3S_4/$CoMo_2S_4$@rGO delivers large specific capacity and exhibits superior rate capability and remarkable cycle stability. These excellent performances are attributed to the special configuration of Co_3S_4/$CoMo_2S_4$@rGO: spinel Co_3S_4/$CoMo_2S_4$ nanoparticles highly dispersed on rGO. It is found that the introduction of suitable content of rGO into the hybrid not only provides an electronically conductive network, but also ensures the formation of spinel nanoparticles that are beneficial for improving cycle stability and rate capability for lithium and sodium ion storage. This hybrid provides a promising alternative anode to graphite for improving energy density of currently commercial LIBs, and a novel anode for the practical applications of SIBs.

Acknowledgements

This work is supported by the National Natural Science Foundation of China (No. 21872058) and the Key Project of Science and Technology in Guangdong Province (No. 2017A010106006).

Electronic Supplementary Material: Supplementary material (XRD analysis, TGA analysis, BET analysis, SEM images, TEM images, EDS mappings, electrochemical data and tables) is available in the online version of this article at https://doi.org/10.1007/s12274-019-2594-2.

References

[1] Wang, H. R.; Huang, Y. S.; Huang, C. F.; Wang, X. S.; Wang, K.; Chen, H. B.; Liu, S. B.; Wu, Y. P.; Xu, K.; Li, W. S. Reclaiming graphite from spent lithium ion batteries ecologically and economically. *Electrochim. Acta* **2019**, *313*, 423–431.

[2] Lin, Z. H.; Li, J. H.; Huang, Q. M.; Xu, K.; Fan, W. Z.; Yu, L.; Xia, Q. B.; Li, W. S. Insights into the Interfacial Instability between carbon-coated SiO anode and electrolyte in lithium-ion batteries. *J. Phys. Chem. C* **2019**, *123*, 12902–12909.

[3] Palomares, V.; Serras, P.; Villaluenga, I.; Hueso, K. B.; Carretero-González, J.; Rojo, T. Na-ion batteries, recent advances and present challenges to become low cost energy storage systems. *Energy Environ. Sci.* **2012**, *5*, 5884–5901.

[4] Wu, S. F.; Wang, W. X.; Li, M. C.; Cao, L. J.; Lyu, F.; Yang, M. Y.; Wang, Z. Y.; Shi, Y.; Nan, B.; Yu, S. C. et al. Highly durable organic electrode for sodium-ion batteries via a stabilized α-C radical intermediate. *Nat. Commun.* **2016**, *7*, 13318.

[5] Yabuuchi, N.; Kubota, K.; Dahbi, M.; Komaba, S. Research development on sodium-ion batteries. *Chem. Rev.* **2014**, *114*, 11636–11682.

[6] Wu, C.; Zhu, Y.; Guan, C.; Jia, C. K.; Qin, W.; Wang, X. Y.; Zhang, K. L. Mesoporous aluminium manganese cobalt oxide with pentahedron structures for energy storage devices. *J. Mater. Chem. A* **2019**, *7*, 18417–18427.

[7] Sun, W. Y.; Li, P.; Liu, X.; Shi, J. J.; Sun, H. M.; Tao, Z. L.; Li, F. J.; Chen, J. Size-controlled MoS_2 nanodots supported on reduced graphene oxide for hydrogen evolution reaction and sodium-ion batteries. *Nano Res.* **2017**, *10*, 2210–2222.

[8] Wang, L. L.; Gu, X. L.; Zhao, L. Y.; Wang, B.; Jia, C. K.; Xu, J. L.; Zhao, Y. F.; Zhang, J. J. ZnO@TiO_2 heterostructure arrays/carbon cloth by charge redistribution enhances performance in flexible anode for Li ion batteries. *Electrochim. Acta* **2019**, *295*, 107–112.

[9] Wang, X. S.; Pan, Z. H.; Wu, Y.; Ding, X. Y.; Hong, X. J.; Xu, G. G.; Liu, M. N.; Zhang, Y. G.; Li, W. S. Infiltrating lithium into carbon cloth decorated with zinc oxide arrays for dendrite-free lithium metal anode. *Nano Res.* 2019, *12*, 525–529.

[10] Wang, Y.; Wang, X. Y.; Li, X. L.; Yu, R. Z.; Chen, M. F.; Tang, K.; Zhang, X. H. The novel P3-type layered $Na_{0.65}Mn_{0.75}Ni_{0.25}O_2$ oxides doped by non-metallic elements for high performance sodium-ion batteries. *Chem. Eng. J.* **2019**, *360*, 139–147.

[11] Yan, Z. C.; Tang, L.; Huang, Y. Y.; Hua, W. B.; Wang, Y.; Liu, R.; Gu, Q. F.; Indris, S.; Chou, S. L.; Huang, Y. H. et al. A hydrostable cathode material based on the layered P2@P3 composite that shows redox behavior for copper in high-rate and long-cycling sodium-ion batteries. *Angew. Chem., Int. Ed.* **2019**, *58*, 1412–1416.

[12] Chen, J.; Li, L. J.; Wu, L.; Yao, Q.; Yang, H. P.; Liu, Z. S.; Xia, L. F.; Chen, Z. Y.; Duan, J. F.; Zhong, S. K. Enhanced cycle stability of $Na_{0.9}Ni_{0.45}Mn_{0.55}O_2$ through tailoring O3/P2 hybrid structures for sodium-ion batteries. *J. Power Sources* **2018**, *406*, 110–117.

[13] Zhang, K.; Park, M.; Zhang, J.; Lee, G. H.; Shin, J.; Kang, Y. M. Cobalt phosphide nanoparticles embedded in nitrogen-doped carbon nanosheets: Promising anode material with high rate capability

and long cycle life for sodium-ion batteries. *Nano Res.* **2017**, *10*, 4337–4350.

[14] Ge, X. F.; Liu, S. H.; Qiao, M.; Du, Y. C.; Li, Y. F.; Bao, J. C.; Zhou, X. S. Enabling superior electrochemical properties for highly efficient potassium storage by impregnating ultrafine sb nanocrystals within nanochannel-containing carbon nanofibers. *Angew. Chem., Int. Ed.* **2019**, *58*, 14578–14583.

[15] Slater, M. D.; Kim, D.; Lee, E.; Johnson, C. S. Sodium-ion batteries. *Adv. Funct. Mater.* **2013**, *23*, 947–958.

[16] Chen, X. Q.; Zhu, Y. M.; Li, B; Hong, P. B.; Luo, X. Y.; Zhong, X. X.; Xing, L. D.; Li, W. S. Porous manganese oxide nanocubes enforced by solid electrolyte interphase as anode of high energy density battery. *Electrochim. Acta* **2017**, *224*, 251–259.

[17] Li, J. B.; Yan, D.; Lu, T.; Yao, Y. F.; Pan, L. K. An advanced CoSe embedded within porous carbon polyhedra hybrid for high performance lithium-ion and sodium-ion batteries. *Chem. Eng. J.* **2017**, *325*, 14–24.

[18] Wang, Y.; Kong, D. Z.; Shi, W. H.; Liu, B.; Sim, G. J.; Ge, Q.; Yang, H. Y. Ice templated free-standing hierarchically WS_2/CNT-rGO aerogel for high-performance rechargeable lithium and sodium ion batteries. *Adv. Energy Mater.* **2016**, *6*, 1601057.

[19] Wu, C.; Zhu, Y.; Ding, M.; Jia, C. K.; Zhang, K. L. Fabrication of plate-like MnO_2 with excellent cycle stability for supercapacitor electrodes. *Electrochim. Acta* **2018**, *291*, 249–255.

[20] Zhao, Q. L.; Gaddam, R. R.; Yang, D. F.; Strounina, E.; Whittaker, A. K.; Zhao, X. S. Pyromellitic dianhydride-based polyimide anodes for sodium-ion batteries. *Electrochim. Acta* **2018**, *265*, 702–708.

[21] Li, D. H.; Yang, D. J.; Yang, X. F.; Wang, Y.; Guo, Z. Q.; Xia, Y. Z.; Sun, S. L.; Guo, S. J. Double-helix structure in carrageenan-metal hydrogels: A general approach to porous metal sulfides/carbon aerogels with excellent sodium-ion storage. *Angew. Chem., Int. Ed.* **2016**, *55*, 15925–15928.

[22] Cai, X.; Lin, H. B.; Zeng, X. W.; Chen, X. Q.; Xia, P.; Luo, X. Y.; Zhong, X. X.; Li, X. P.; Li, W. S. Facile synthesis of porous iron oxide rods coated with carbon as anode of high energy density lithium ion battery. *Electrochim. Acta* **2016**, *191*, 767–775.

[23] Zhu, J. X.; Tang, C. J.; Zhuang, Z. C.; Shi, C. W.; Li, N. R.; Zhou, L.; Mai, L. Q. Porous and low-crystalline manganese silicate hollow spheres wired by graphene oxide for high-performance lithium and sodium storage. *ACS Appl. Mater. Interfaces* **2017**, *9*, 24584–24590.

[24] Li, X. M.; Feng, Z. X.; Zai, J. T.; Ma, Z. F.; Qian, X. F. Incorporation of Co into MoS_2/graphene nanocomposites: One effective way to enhance the cycling stability of Li/Na storage. *J. Power Sources* **2018**, *373*, 103–109.

[25] Cherian, C. T.; Reddy, M. V.; Haur, S. C.; Chowdari, B. V. R. Interconnected network of $CoMoO_4$ submicrometer particles as high capacity anode material for lithium ion batteries. *ACS Appl. Mater. Interfaces* **2013**, *5*, 918–923.

[26] Li, M.; Xu, S. H.; Cherry, C.; Zhu, Y. P.; Wu, D. J.; Zhang, C.; Zhang, X. L.; Huang, R.; Qi, R. J.; Wang, L. W. et al. Hierarchical 3-dimensional $CoMoO_4$ nanoflakes on a macroporous electrically conductive network with superior electrochemical performance. *J. Mater. Chem. A* **2015**, *3*, 13776–13785.

[27] Yu, H.; Guan, C.; Rui, X. H.; Ouyang, B.; Yadian, B. L.; Huang, Y. Z.; Zhang, H.; Hoster, H. E.; Fan, H. J.; Yan, Q. Y. Hierarchically porous three-dimensional electrodes of $CoMoO_4$ and $ZnCo_2O_4$ and their high anode performance for lithium ion batteries. *Nanoscale* **2014**, *6*, 10556–10561.

[28] Yao, J. Y.; Gong, Y. J.; Yang, S. B.; Xiao, P.; Zhang, Y. H.; Keyshar, K.; Ye, G. L.; Ozden, S.; Vajtai, R.; Ajayan, P. M. $CoMoO_4$ nanoparticles anchored on reduced graphene oxide nanocomposites as anodes for long-life lithium-ion batteries. *ACS Appl. Mater. Interfaces* **2014**, *6*, 20414–20422.

[29] Zhang, L. H.; Zhu, S. Q.; Cao, H.; Hou, L. R.; Yuan, C. Z. Hierarchical porous $ZnMn_2O_4$ hollow nanotubes with enhanced lithium storage toward lithium-ion batteries. *Chemistry* **2015**, *21*, 10771–10777.

[30] Chen, X. Q.; Zhang, Y. M.; Lin, H. B.; Xia, P.; Cai, X.; Li, X. G.; Li, X. P.; Li, W. S. Porous $ZnMn_2O_4$ nanospheres: Facile synthesis through microemulsion method and excellent performance as anode of lithium ion battery. *J. Power Sources* **2016**, *312*, 137–145.

[31] Zhou, L.; Zhao, D. Y.; Lou, X. W. Double-shelled $CoMn_2O_4$ hollow microcubes as high-capacity anodes for lithium-ion batteries. *Adv. Mater.* **2012**, *24*, 745–748.

[32] Yu, L.; Guan, B. Y.; Xiao, W.; Lou, X. W. D. Formation of yolk-shelled Ni-Co mixed oxide nanoprisms with enhanced electrochemical performance for hybrid supercapacitors and lithium ion batteries. *Adv. Energy Mater.* **2015**, *5*, 1500981.

[33] Yang, D. F.; Zhao, Q. L.; Huang, L. Q.; Xu, B. H.; Kumar, N. A.; Zhao, X. S. Encapsulation of $NiCo_2O_4$ in nitrogen-doped reduced graphene oxide for sodium ion capacitors. *J. Mater. Chem. A* **2018**, *6*, 14146–14154.

[34] Yuan, C. Z.; Li, J. Y.; Hou, L. R.; Zhang, X. G.; Shen, L. F.; Lou, X. W. Ultrathin mesoporous $NiCo_2O_4$ nanosheets supported on Ni foam as advanced electrodes for supercapacitors. *Adv. Funct. Mater.* **2012**, *22*, 4592–4597.

[35] Saravanakumar, B.; Wang, X. S.; Zhang, W. G.; Xing, L. D.; Li, W. S. Holey two dimensional manganese cobalt oxide nanosheets as a high-performance electrode for supercapattery. *Chem. Eng. J.* **2019**, *373*, 547–555.

[36] Wang, X. J.; Cao, K. Z.; Wang, Y. J.; Jiao, L. F. Controllable N-doped $CuCo_2O_4$@C film as a self-supported anode for ultrastable sodium-ion batteries. *Small* **2017**, *13*, 1700873.

[37] Zhu, C. B.; Mu, X. K.; van Aken, P. A.; Yu, Y.; Maier, J. Single-layered ultrasmall nanoplates of MoS_2 embedded in carbon nanofibers with excellent electrochemical performance for lithium and sodium storage. *Angew. Chem., Int. Ed.* **2014**, *53*, 2152–2156.

[38] Chang, K.; Chen, W. X. L-cysteine-assisted synthesis of layered MoS_2/graphene composites with excellent electrochemical performances for lithium ion batteries. *Acs Nano* **2011**, *5*, 4720–4728.

[39] Tu, F. Z.; Han, Y.; Du, Y. C.; Ge, X. F.; Weng, W. S.; Zhou, X. S.; Bao, J. C. Hierarchical nanospheres constructed by ultrathin MoS_2 nanosheets braced on nitrogen-doped carbon polyhedra for efficient lithium and sodium storage. *ACS Appl. Mater. Interfaces* **2019**, *11*, 2112–2119.

[40] Wang, Y.; Kong, D. Z.; Huang, S. Z.; Shi, Y. M.; Ding, M.; von Lim, Y.; Xu, T. T.; Chen, F. M.; Li, X. J.; Yang, H. Y. 3D carbon foam-supported WS_2 nanosheets for cable-shaped flexible sodium ion batteries. *J. Mater. Chem. A* **2018**, *6*, 10813–10824.

[41] Li, X. M.; Zai, J. T.; Xiang, S. J.; Liu, Y. Y.; He, X. B.; Xu, Z. Y.; Wang, K. X.; Ma, Z. F.; Qian, X. F. Regeneration of metal sulfides in the delithiation process: The key to cyclic stability. *Adv. Energy Mater.* **2016**, *6*, 1601056.

[42] Tan, Y. B.; Liang, M.; Lou, P. L.; Cui, Z. H.; Guo, X. X.; Sun, W. W.; Yu, X. B. *In situ* fabrication of CoS and NiS nanomaterials anchored on reduced graphene oxide for reversible lithium storage. *ACS Appl. Mater. Interfaces* **2016**, *8*, 14488–14493.

[43] Sun, D.; Ye, D. L.; Liu, P.; Tang, Y. G.; Guo, J.; Wang, L. Z.; Wang, H. Y. MoS_2/graphene nanosheets from commercial bulky MoS_2 and graphite as anode materials for high rate sodium-ion batteries. *Adv. Energy Mater.* **2018**, *8*, 1702383.

[44] Xiong, X. H.; Yang, C. H.; Wang, G. H.; Lin, Y. W.; Ou, X.; Wang, J. H.; Zhao, B.; Liu, M. L.; Lin, Z.; Huang, K. SnS nanoparticles electrostatically anchored on three-dimensional N-doped graphene as an active and durable anode for sodium-ion batteries. *Energy Environ. Sci.* **2017**, *10*, 1757–1763.

[45] Li, X. M.; Qian, T. Y.; Zai, J. T.; He, K.; Feng, Z. X.; Qian, X. F. Co stabilized metallic $1T_d$ MoS_2 monolayers: Bottom-up synthesis and enhanced capacitance with ultra-long cycling stability. *Mater. Today Energy* **2018**, *7*, 10–17.

[46] Zhu, Y. Y.; Ramasse, Q. M.; Brorson, M.; Moses, P. G.; Hansen, L. P.; Kisielowski, C. F.; Helveg, S. Visualizing the stoichiometry of industrial-style Co-Mo-S catalysts with single-atom sensitivity. *Angew. Chem., Int. Ed.* **2014**, *53*, 10723–10727.

[47] Zhu, H.; Zhang, J. F.; Yanzhang, R. P.; Du, M. L.; Wang, Q. F.; Gao, G. H.; Wu, J. D.; Wu, G. M.; Zhang, M.; Liu, B. et al. When cubic cobalt sulfide meets layered molybdenum disulfide: A core-shell

system toward synergetic electrocatalytic water splitting. *Adv. Mater.* **2015**, *27*, 4752–4759.

[48] Yang, X. J.; Sun, H. M.; Zan, P.; Zhao, L. J.; Lian, J. S. Growth of vertically aligned Co_3S_4/$CoMo_2S_4$ ultrathin nanosheets on reduced graphene oxide as a high-performance supercapacitor electrode. *J. Mater. Chem. A* **2016**, *4*, 18857–18867.

[49] Liao, Y. Q.; Huang, Y. L.; Shu, D.; Zhong, Y. Y.; Hao, J. N.; He, C.; Zhong, J.; Song, X. N. Three-dimensional nitrogen-doped graphene hydrogels prepared via hydrothermal synthesis as high-performance supercapacitor materials. *Electrochim. Acta* **2016**, *194*, 136–142.

[50] Yang, J.; Xuan, H. C.; Yang, G. H.; Liang, T.; Han, X. K.; Gao, J. H.; Xu, Y. K.; Xie, Z. G.; Han, P. D.; Wang, D. H. et al. Formation of a flower-like Co-Mo-S on reduced graphene oxide composite on nickel foam with enhanced electrochemical capacitive properties. *ChemElectroChem* **2018**, *5*, 3748–3756.

[51] Chen, T.; Zhang, Z. W.; Cheng, B. R.; Chen, R. P.; Hu, Y.; Ma, L. B.; Zhu, G. Y.; Liu, J.; Jin, Z. Self-templated formation of interlaced carbon nanotubes threaded hollow Co_3S_4 nanoboxes for high-rate and heat-resistant lithium-sulfur batteries. *J. Am. Chem. Soc.* **2017**, *139*, 12710–12715.

[52] Wu, Y. Z.; Meng, J. S.; Li, Q.; Niu, C. J.; Wang, X. P.; Yang, W.; Li, W.; Mai, L. Q. Interface-modulated fabrication of hierarchical yolk-shell Co_3O_4/C dodecahedrons as stable anodes for lithium and sodium storage. *Nano Res.* **2017**, *10*, 2364–2376.

[53] Li, Z. Q.; Zhang, L. Y.; Ge, X. L.; Li, C. X.; Dong, S. H.; Wang, C. X.; Yin, L. W. Core-shell structured CoP/FeP porous microcubes interconnected by reduced graphene oxide as high performance anodes for sodium ion batteries. *Nano Energy* **2017**, *32*, 494–502.

[54] Chen, R. J.; Zhao, T.; Wu, W. P.; Wu, F.; Li, L.; Qian, J.; Xu, R.; Wu, H. M.; Albishri, H. M.; Al-Bogami, A. S. et al. Free-standing hierarchically sandwich-type tungsten disulfide nanotubes/graphene anode for lithium-ion batteries. *Nano Lett.* **2014**, *14*, 5899–5904.

[55] Niu, F. E.; Yang, J.; Wang, N. N.; Zhang, D. P.; Fan, W. L.; Yang, J.; Qian, Y. T. $MoSe_2$-covered N,P-doped carbon nanosheets as a long-life and high-rate anode material for sodium-ion batteries. *Adv. Funct. Mater.* **2017**, *27*, 1700522.